

# How Should Iron and Titanium be Combined in Oxides to Improve Photoelectrochemical Properties?

*Sarah Petit<sup>1</sup>, Sigismund T.A.G. Melissen<sup>2</sup>, Lorraine Duclaux<sup>1</sup>, Moulay T. Sougrati<sup>3</sup>, Tangui Le Bahers<sup>2</sup>, Philippe Sautet†<sup>2</sup>, Damien Dambournet<sup>4</sup>, Olaf Borkiewicz<sup>5</sup>, Christel Laberty-Robert<sup>1</sup>, and Olivier Durupthy\*<sup>1</sup>*

1 Sorbonne Universités, UPMC Univ Paris 06, CNRS, Collège de France, Laboratoire de Chimie de la Matière Condensée de Paris, 4 place Jussieu, 75005 Paris, France.

2 Université de Lyon, CNRS, École Normale Supérieure de Lyon,

Université Claude Bernard Lyon 1, Laboratoire de Chimie, UMR 5182

46 Allée d'Italie, 69342 Lyon CEDEX, France

3 ICGM – UMR5253 – Equipe AIME, Université Montpellier II, 2 Place Eugène Bataillon – CC1502, 34095 Montpellier CEDEX 5, France.

4 Sorbonne Universités, UPMC Univ Paris 06, CNRS, UMR 8234, PHENIX, F-75005 Paris, France

5 X-ray Science Division, Advanced Photon Source, Argonne National Laboratory, Argonne, Illinois, USA

## ABSTRACT

We discuss here for the first time how to combine iron and titanium metal ions to achieve a high photo-electrochemical activity for TiO<sub>2</sub>-based photo-anodes in water splitting devices. To do so, a wide range of photoelectrode materials with tailored Ti/Fe ratio and element vicinity were synthesized by using the versatility of aqueous sol-gel chemistry in combination with a microwave-assisted crystallization process. At low ferric concentrations, single phase TiO<sub>2</sub> anatase doped with various Fe amounts were prepared. Strikingly, at higher ferric concentrations, we observed the concomitant crystallization of two polymorphs of Fe<sub>2</sub>TiO<sub>5</sub>. The as-synthesized compounds were tested as photoelectrode and compared with pure nanoparticles of TiO<sub>2</sub>, Fe<sub>2</sub>TiO<sub>5</sub> and  $\alpha$ - or  $\gamma$ -Fe<sub>2</sub>O<sub>3</sub> and with corresponding nanocomposites. When TiO<sub>2</sub> is slightly doped by Fe, the performance of this photo-electrode improves particularly in the low-bias region (< 1.0 V vs. reversible hydrogen electrode.) The photoanode exhibits a higher photocurrent than nanocomposite with TiO<sub>2</sub>/Fe<sub>2</sub>O<sub>3</sub> and FeTi<sub>2</sub>O<sub>5</sub>, and more cathodic onset potential. The former can be partly explained by a lower bandgap and a hole with a longer lifetime. For the latter, we propose that the nature of the heterojunction impacts charge carrier recombination. The results presented herein not only answer whether iron and titanium should be combined in the same structure or into heterostructured systems, but also on the importance of the arrangement of ions in the structure to improve the performances of the photoanode.

Keywords. pseudo-brookite, photoanode, water splitting, heterojunctions, “*chimie-douce*”.

## 1. Introduction

One of the grand challenges for the 21<sup>st</sup> century is to secure the availability of energy on demand on the terawatt scale. Moreover, environmental concerns result in the need for renewable energy sources to satisfy this demand. The direct photoelectrochemical (PEC) conversion of solar energy into storable fuels, which is based on cheap and earth-abundant semiconductors and catalysts, has the potential to satisfy these requirements.<sup>1-6</sup> Metal-oxide semiconductors are particularly appealing candidates for practical applications because of their low cost, nontoxicity, abundance, and stability toward corrosion.

For application in a water splitting device, a semiconductor must fulfill several requirements based on the microscopic steps involved in the working principle. First, the semiconductor must absorb sunlight efficiently to create an exciton. This property is governed by the bandgap ( $E_g$ ) and the absorption coefficient ( $\alpha$ ). Then, the exciton is dissociated yielding a free electron and a free hole. Spontaneous dissociation is facile if the exciton binding energy ( $E_b$ ) in the material is lower than the thermal energy at room temperature (25 meV). These free charges must diffuse toward the active sites for catalysis. The diffusion of charge carriers is characterized by the electron and hole mobilities ( $\mu$ ), which are themselves related to the effective masses of the charge carriers ( $m^*$ ). Then, the valence band (VB) and conduction band (CB) must be positioned such, that they straddle the redox potentials of the target reactions.<sup>7, 8</sup> If the active sites are on another material, the band positions must be adapted to allow the charge transfer between the two systems thermodynamically. The efficiency of this final step is not only governed by bulk properties of the semiconductor, but also by the electronic structure of the interface. In addition to these requirements on the microscopic properties of the bulk or the interface, other more

general constraints must be satisfied, such as the chemical stability in working conditions and the low cost of the materials.

Among the different materials already tested,<sup>9</sup> TiO<sub>2</sub> and Fe<sub>2</sub>O<sub>3</sub> have attracted a lot of attention in PEC water splitting applications, since they fulfill several of these requirements.<sup>10-12</sup> TiO<sub>2</sub> has been the first material tested for water oxidation.<sup>13, 14</sup> The TiO<sub>2</sub> absorption edge is 3.2 eV, allowing only 4% of the incident solar energy to be absorbed at best.<sup>14-16</sup> Its CB lies slightly above the hydrogen evolution redox potential, potentially decreasing the onset potential. The electron mobility of TiO<sub>2</sub> in a nanoparticle (NP) film is about 0.01 cm<sup>2</sup>·V<sup>-1</sup>·sec<sup>-1</sup>, which is low compared to the mobility observed in monocrystals of 1 cm<sup>2</sup>·V<sup>-1</sup>·sec<sup>-1</sup>.<sup>17</sup> Accordingly, TiO<sub>2</sub> suffers from two major limitations which compromise high photon-to-hydrogen conversion efficiency: its wide bandgap and its fast electron–hole recombination. Lately, hematite has emerged as a more promising material due to its suitable bandgap of 2.1 eV, which corresponds to a maximum theoretical air mass 1.5 global (AM 1.5 G) photocurrent density of 12.3 mA·cm<sup>-2</sup>.<sup>18</sup> Hematite also has an excellent chemical stability in a broad pH range and is naturally abundant, nontoxic and cheap. The hematite conduction band minimum (CBM) and valence band maximum (VBM) are located at -0.3 V and 1.7 V vs. reversible hydrogen electrode (RHE) at pH = 0, respectively.<sup>8, 10</sup> However, the reported water oxidation efficiencies for hematite to date are notoriously lower than the predicted maximum value despite intense efforts.<sup>18</sup> This is caused by two principal limiting physical properties: the short lifetime of the photogenerated charge carriers ( $\leq 10$  ps), and the low mobility of the minority carriers (0.2 cm<sup>2</sup>·V<sup>-1</sup>·sec<sup>-1</sup>).<sup>18</sup> The combined effect is that the minority carrier (hole) diffusion length is only 2-4 nm, whereas full absorption of the incident light requires much thicker films due to the indirect nature of the bandgap (the penetration depth of light is  $\sim 118$  nm at a wavelength of 550 nm).<sup>18</sup>

This short literature overview underlines that no single material, whether  $\text{Fe}_2\text{O}_3$  or  $\text{TiO}_2$ , fulfilled all the criteria for efficient water oxidation. To overcome these intrinsic shortcomings, different approaches have been explored in the literature. For example, the modification of the  $\text{TiO}_2$  surface with a small bandgap semiconductor has been proven to enhance the photocatalytic activity.<sup>19, 20</sup> Another approach consists of tuning the optical and photoelectrochemical (PEC) properties by element doping.<sup>21</sup> For example, ferric doping of  $\text{TiO}_2$  lowers the bandgap from 3.2 to 1.9 eV, depending on the Fe content and the synthesis procedure.<sup>22, 23</sup> However, high doping levels often lead to heterogeneous materials.<sup>24, 25</sup> Their functionality is then the result of both the bulk properties of the various components and their interface properties. We note that some reports in the literature highlight the benefit of designing heterojunctions to enhance the charge separation.<sup>25-28</sup> However, none of them studied together the impact of doping level, atoms ordering and heterostructures formation in the Ti-Fe-O system get high photo(electrochemical) efficiency.

All in all, good photoelectrode material must contain i) a bulk semi-conductor structure that efficiently harvests photons and allows their conversion into mobile charge carriers, titanium oxide structures being particularly efficient in that case; ii) appropriate surface catalytic sites, iron (III) being *a priori* better suited. The issue that is still to be answered is the elements mixing level coupled with the doping level that provide the best results. In other words, can  $\text{Fe}_2\text{TiO}_5$  alone fulfill those conditions, is a low iron doping of titanium oxide enough or is it mandatory to combine metal oxide nanoparticles with completely different chemical compositions?

The goals of this article are to provide original syntheses of Ti-Fe-O nanomaterials with the iron and the titanium atoms combined in the same structure or into heterostructured nanocomposites and to correlate the structural aspects of the materials used as photoanode with their efficiency

for water oxidation. The huge versatility of aqueous sol-gel chemistry and more precisely that of iron and titanium metal ions is the perfect toolbox to prepare a wide range of photoelectrode materials with tailored Ti/Fe ratio and element vicinity. We have prepared single phase  $\text{TiO}_2$ -anatase ( $\text{TiO}_2\text{-A}$ ) doped with various amounts of ferric ions,  $\text{Fe}_2\text{TiO}_5$  nanoparticles featuring two structural arrangements, *i.e.* a heterostructured system. We have also mixed phase pure NPs of  $\text{TiO}_2$ ,  $\text{Fe}_2\text{TiO}_5$  and  $\text{Fe}_2\text{O}_3$  hematite or maghemite to test their efficiency as photoelectrode material.

The PEC activities of the different pure phase and heterostructured systems were recorded and rationalized according to the known relative position of electronic bands and the charge dynamics in the different components. Additionally, an extensively tested theoretical approach<sup>29-33</sup> was invoked to provide key data on the bulk properties of the different pure semi-conductors. This study is the first complete study on the PEC activity of the whole Fe-Ti oxide composition range.

The manuscript is organized as follows. The methodology section is dedicated to the presentation of the experimental and computational details. In the first part of the results, the Density Functional Theory (DFT) calculations of the main  $\text{TiO}_2$ ,  $\text{Fe}_2\text{O}_3$  and  $\text{Fe}_2\text{TiO}_5$  phases will be presented in order to understand the ability of these materials in water splitting devices. Subsequently, structural and morphological characterizations of the different synthesized systems are presented. The PEC activities are then determined for each material. Finally, in a discussion confronting both theoretical and experimental results we explain the relative efficiency of the different systems.

## **2. Methodology**

## 2.1 Experimental setup

### 2.1.1 Nanoparticle syntheses

Preliminary studies have been performed with all the combinations of Fe(II)/(III) and Ti(III)/(IV) precursors in order to form mixed oxides. The best results were achieved with Fe (III) salts and Ti (IV) precursors.

The combination of Fe(III) and Ti(IV) oxides was created according to two different synthetic pathways. First, a crystallite structure involving both metal ions was obtained from the sol-gel reaction of the corresponding salts in aqueous solution. Alternatively, the composites were obtained through the grinding of a mixture of pure nanoparticles of  $\text{TiO}_2$ ,  $\text{Fe}_2\text{TiO}_5$ ,  $\alpha\text{-Fe}_2\text{O}_3$  and  $\gamma\text{-Fe}_2\text{O}_3$ . The initial particles were synthesized through a microwave assisted process described below.

*TiO<sub>2</sub> anatase.*  $\text{TiO}_2$  particles were obtained through the hydrothermal treatment of an aqueous  $\text{TiCl}_4$  solution with a pH set to 6 according to a previously described method.<sup>34</sup> A stock solution with Ti(IV) ion concentration of  $1.0 \text{ mol}\cdot\text{L}^{-1}$  was prepared by dilution of  $\text{TiCl}_4$  in  $\text{HCl}$  ( $3 \text{ mol}\cdot\text{L}^{-1}$ ) solution. Then, 100 mL of the stock solution were introduced in 200 mL of Milli-Q water, the pH was set to 6 by addition of sodium hydroxide solution ( $[\text{NaOH}] = 3 \text{ mol}\cdot\text{L}^{-1}$ ) and the sample volume was increased to 500 mL with Milli-Q water to obtain a Ti(IV) ion concentration of  $0.2 \text{ mol}\cdot\text{L}^{-1}$  in the reacting medium. A white sol immediately appeared; aliquots of this suspension were transferred in Teflon cups and heated in autoclaves for 1 h at  $200 \text{ }^\circ\text{C}$  using a microwave oven (Synthos3000, Anton Paar). The resulting precipitate was collected by centrifugation, washed twice with water, then with nitric acid ( $[\text{HNO}_3] = 3 \text{ mol}\cdot\text{L}^{-1}$ ) and at least one additional time with water. The obtained powders were dried under dry air flow overnight.

*Fe doped TiO<sub>2</sub> anatase.* The former protocol was slightly modified to introduce various amounts of Fe (III) in the final product. The total metal ion concentration was maintained at 0.2 mol·L<sup>-1</sup> and the targeted Fe(III) atomic ratio was varied between 5 and 66 %. The appropriate amount of the Ti(IV) stock solution and solid ferric nitrate nonahydrate (Fe(NO<sub>3</sub>)<sub>3</sub>·9H<sub>2</sub>O) were introduced in 200 mL of Milli-Q water to form a clear yellow solution. Sodium hydroxide solution ([NaOH] = 3 mol·L<sup>-1</sup>) was then added to adjust the pH to 2-6 and the sample volume was increased to 500 mL with Milli-Q water. A brownish precipitate is obtained, hydrothermally treated in the microwave oven and washed the same way as the pure TiO<sub>2</sub> sample. The samples obtained with a pH of the reacting medium of 6 are denoted by acronyms indicating the added iron content in at.%, for example TiO<sub>2</sub>-10%Fe. For reacting media with other pH values, this is indicated at the end of the sample name.

*Fe<sub>2</sub>TiO<sub>5</sub>.* Fe<sub>2</sub>TiO<sub>5</sub> nanoparticles used for the mixing were obtained according to the former protocol with a well-defined set of parameters. The metal precursors were introduced with a relative Ti:Fe atomic ratio of 1:1 and the pH of the reactive medium was fixed at 6 with NaOH.

*α-Fe<sub>2</sub>O<sub>3</sub> Hematite.* The preparation protocol is similar to that of iron doped titania particles, except that Fe(NO<sub>3</sub>)<sub>3</sub> is the only metal ion source used and the pH of the reacting medium was not fixed with NaOH solution. The hydrolysis of the ferric precursor acidified the aqueous solution to a pH of around 2. A reddish precipitate was obtained.

*γ-Fe<sub>2</sub>O<sub>3</sub> Maghemite.* The particles were synthesized according to an earlier published method using microwave assisted heating in order to reduce the aging time.<sup>35</sup> First, 50 mL of a 0.05 mol·L<sup>-1</sup> ferrous solution prepared from FeSO<sub>4</sub>·7H<sub>2</sub>O and 100 mL of a 0.05 mol·L<sup>-1</sup> ferric solution prepared from FeCl<sub>3</sub>·6H<sub>2</sub>O were mixed together. Then, the pH of the reacting medium was maintained at 12 by adding small amounts of a NaOH solution. The obtained colloidal solution



was heated in a microwave oven for 25 min at 150 °C. Finally, the dark brown precipitate was washed twice with water and dried under air flow.

### **2.1.2 Nanoparticle Characterizations**

UV-visible diffuse reflectance spectra (DRS) of the samples were recorded on a Varian-Cary 5000 spectrometer with integrating sphere from 300 to 800 nm. Powder X-ray diffraction (XRD) measurements were performed with a Brücker D8 X-ray diffractometer operating in the Bragg-Brentano reflection mode using Cu K $\alpha$  radiation. The data were collected in the 20 – 80° 2 $\theta$  range with 0.02° steps and a counting time of 5 s per step. Transmission electron micrographs (TEMs) were obtained using a Tecnai spirit G2 apparatus operating at 120 kV. Samples were prepared by evaporating dilute suspensions in ethanol onto carbon-coated grids. Relative iron and titanium atomic composition of the samples was determined with a scanning electron microscope (Hitachi S-3400N) equipped with energy-dispersive X-ray spectroscopy (EDX, Oxford Instruments - X-max).

Total scattering data were collected at the 11-ID-B beamline at the Advanced Photon Source at Argonne National Laboratory, using high energy X-rays ( $\lambda = 0.2128 \text{ \AA}$ ) to high values of momentum transfer  $Q_{\text{max}} = 22 \text{ \AA}^{-1}$ .<sup>36, 37</sup> One-dimensional diffraction data were obtained by integrating the raw 2D total scattering data in Fit2D.<sup>38</sup> Pair distribution functions (PDFs)  $G(r)$  were extracted from the background and Compton scattering corrected data following Fourier transform within PDFgetX2.<sup>39</sup> The PDFs were subsequently modeled using PDFgui.<sup>40</sup>

### **2.1.3 Film preparation**

As photoanode, we synthesized 30  $\mu\text{m}$  mesoporous films (*cf.* Figure SI-1) by tape casting. 37 wt.% of the inorganic powders was dispersed in ethanol with 5 wt.% of ethylene glycol and 0.5 wt.% of Triton X. The ethanol suspensions were mixed in an ultrasonic bath for ½ h before

deposition. The ethanol suspensions were then deposited directly onto a fluoride tin oxide (FTO) substrate to yield homogeneous thick films. The substrates used are TEC-15 FTO-coated glass (15Ω/sq, Asahi, Co). After the deposition, the thick-films were annealed for 3 min. at 300 °C in air to decompose the organic material and to further improve the particle-particle contact.

#### **2.1.4 Photo-electrochemical characterizations**

PEC characterization was carried out in an aqueous solution 1 mol·L<sup>-1</sup> NaOH (pH = 14). The solution was purged with nitrogen prior to and during the measurements to remove any dissolved oxygen. The working area of the electrodes exposed to the electrolyte was 28.5 mm<sup>2</sup> for all samples. The potential of the working electrode was controlled by potentiostat (Modulab, Ametek). In three-electrode measurements, a Pt wire and an Ag/AgCl electrode (Asashi, saturated AgCl solution) were used as the counter and reference electrodes, respectively. Cyclic voltammetry measurements were performed with a scan rate of 20 mV·s<sup>-1</sup>. Light photocurrent measurements were performed using the visible range of a 300 W Xe-Lamp (Oriel and a UV filter with a 400 nm wavelength cutoff) providing a power density of 300 mW·cm<sup>-2</sup> at the surface of the electrode. Electrical contact to the sample was made using a copper tape. For the cyclic voltammograms represented below, the potentials are referenced to RHE according to the following equation:

$$E \text{ (V/RHE)} = E \text{ (V/Ag/AgCl)} + E^{\circ}_{\text{Ag/AgCl}} + 0.059 \text{ pH.} \quad (1)$$

### **2.2 Computational details**

#### **2.2.1 Density Functional Theory (DFT) Calculations**

Geometry optimizations and frequency calculations were performed using the CRYSTAL14 code, due to its efficiency when doing calculations with hybrid functionals using Gaussian Type Orbitals.<sup>41, 42</sup> All optimized structures were characterized as minima on the potential energy

surface by vibrational analysis. The all-electron 86-411G(2d) basis sets for Fe<sup>43</sup> and Ti<sup>44</sup> and an 8-41G(d) basis set for O were used.<sup>44</sup> All calculations, except for electronic structure calculations, were performed using the hybrid PBE0 functional,<sup>45</sup> using an 8×8×4 K-point mesh<sup>46</sup> for Fe<sub>2</sub>TiO<sub>5</sub> and a 12×12×12 mesh for α-Fe<sub>2</sub>O<sub>3</sub>. Electronic structure calculations were performed with a 10×10×6 mesh for Fe<sub>2</sub>TiO<sub>5</sub> and a 24×24×24 mesh for α-Fe<sub>2</sub>O<sub>3</sub> and using the range-separated HSE06 functional<sup>47, 48</sup> with  $\omega = 0.11 \text{ a}_0^{-1}$ ,<sup>49</sup> based on its positive comparison in terms of speed and accuracy with other hybrid functionals found here and reported earlier.<sup>50-52</sup> (HSE06 reduces to PBE0 when setting  $\omega$  to zero.) The dielectric constant  $\epsilon_r$  is the sum of a vibrational contribution  $\epsilon_{\text{vib}}$  and an optical contribution  $\epsilon_\infty$ . The first term  $\epsilon_{\text{vib}}$  was computed invoking the harmonic approximation to the lattice potential, with infrared intensities calculated using the Berry phase method.<sup>53</sup> The second term was computed using the Coupled-Perturbed Kohn-Sham (CPKS, although sometimes the acronym CPHF is used) approach.<sup>54-56</sup> The individual terms were calculated by taking the geometric mean of the diagonal elements of the (diagonalized) dielectric tensors.<sup>57</sup>

## 2.2.2 Bulk properties calculations

The bulk properties computed to understand the semiconductors' capacities for photocatalytic reactions are the bandgap (noted  $E_g$ ), the dielectric constant (noted  $\epsilon_r$ ), the effective masses (noted  $m^*$ ) and the exciton binding energy (noted  $E_b$ ). The way to compute all these properties were presented in the following article<sup>52</sup> and used to compute properties of several families of semiconductors including oxides, sulfides, nitrides and halides. It can just be reminded that first the total dielectric constant ( $\epsilon_r$ ) is the sum of the electronic ( $\epsilon_\infty$ ) and the vibrational contribution ( $\epsilon_{\text{vib}}$ ) and then the exciton binding energy is computed in the framework of the Wannier model using the average values of  $m^*$  and  $\epsilon_r$ . This model is generally well adapted for delocalized

excitons (large dielectric constant and low effective masses), which is usually the case for inorganic semiconductors.

### 3 Results and discussion

#### 3.1 Bulk properties of the semiconductors

The materials used for the work presented in this manuscript fulfill several requirements of the bulk semiconductors properties presented in the introduction. This verification has been performed using the DFT calculations presented here.

*Geometry optimizations.*  $\alpha$ -Fe<sub>2</sub>O<sub>3</sub> (crystallographic cell in Figure 1a) was optimized in the  $R\bar{3}c$  geometry as given by Adelstein *et al.*,<sup>58</sup> using the conventional Anti-Ferromagnetic (AFM) spin configuration, reducing the symmetry to  $R\bar{3}$ .<sup>59</sup> TiO<sub>2</sub> (crystallographic cell in Figure 1b) was optimized in the anatase structure at the same level of theory as in a previous publication.<sup>52</sup> For Fe<sub>2</sub>TiO<sub>5</sub> (space group: *Ccmm*), the orthorhombic pseudo-brookite structure with ordered distribution of Fe was chosen and several spin isomers were investigated, since the exact spin state of the Fe(III) atoms is unknown. Figure 1c presents the structure of the most stable spin state found for Fe<sub>2</sub>TiO<sub>5</sub>. This is an anti-ferromagnetic spin state (AFM). The calculations revealed that several spin states (all AFM) are close in energy (see supporting information for more details). The ferromagnetic structure was significantly less stable (~1.1 eV/unit cell) than the AFM ones. The cell parameters of all the semiconductors are presented in Table 1. The larger discrepancy on a cell parameter between DFT and experiment is around 1.05%, which is the standard discrepancy at this level of theory.

	$\alpha$ -Fe <sub>2</sub> O <sub>3</sub>	TiO <sub>2</sub>	Fe <sub>2</sub> TiO <sub>5</sub>
	$a / \text{\AA}$ $b / \text{\AA}$	$a / \text{\AA}$ $b / \text{\AA}$	$a / \text{\AA}$ $b / \text{\AA}$ $c / \text{\AA}$

Expt'l	5.04	13.77	3.78	9.51	9.79	3.73	9.98
Calc'd	5.04	13.70	3.77	9.61	9.86	3.75	9.90

Table 1. Experimental and computed cell parameters of  $\alpha$ -Fe<sub>2</sub>O<sub>3</sub>, TiO<sub>2</sub>, and Fe<sub>2</sub>TiO<sub>5</sub><sup>52,60,61</sup>

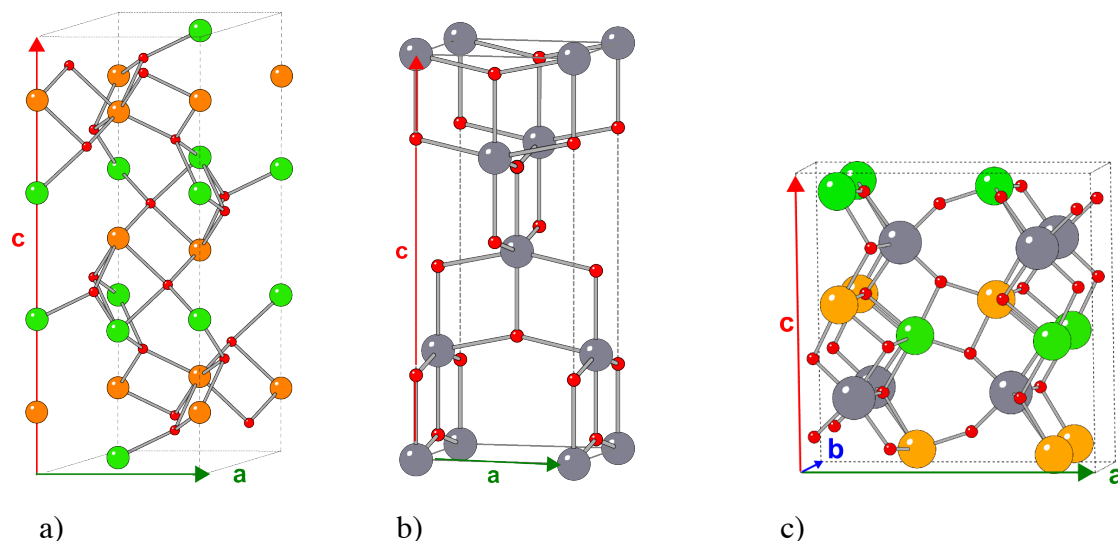


Figure 1: Representation of the conventional crystallographic cells of (a)  $\alpha$ -Fe<sub>2</sub>O<sub>3</sub>, (b) TiO<sub>2</sub>, and (c) Fe<sub>2</sub>TiO<sub>5</sub>. Red, grey, orange and green atoms correspond to O, Ti, Fe (spin up) and Fe (spin down) atoms respectively.

*Electronic properties.* The density of states (DOS) of the compounds are presented on Figure 2. It appears that the valence bands is largely made up of the O atoms' orbitals while the conduction bands originate from Fe orbitals for  $\alpha$ -Fe<sub>2</sub>O<sub>3</sub> and Fe<sub>2</sub>TiO<sub>5</sub> and from Ti atoms for TiO<sub>2</sub>. All relevant computed properties for photocatalysis are presented in Table 2. While the bandgap computed for TiO<sub>2</sub> is relatively close to the experimental one, the  $E_g$  computed for Fe-containing semiconductors is overestimated.<sup>62</sup> Unfortunately, this is the expected behavior when hybrid functionals are applied to materials having partially filled d-orbitals. A GGA+U approach<sup>63</sup> could solve this problem, but GGA functionals are unreliable for the calculation of other properties

explaining the choice for hybrid functionals as a compromise. About the effective masses, for  $\alpha$ - $\text{Fe}_2\text{O}_3$ , values for  $m_e$  of  $\sim 3.5$  were found, whereas for  $m_h$  values of  $\sim 1$  were found, consistent with findings in the literature<sup>64,65</sup> that attribute the heavy electron mass to the strong localization of the VB on O,<sup>10</sup> confirming our approach. The anisotropy of the charge carrier mobilities in  $\alpha$ - $\text{Fe}_2\text{O}_3$  can be explained by Hund's rule,<sup>10</sup> that hinders charge carrier mobility in the [001] direction, where the spins are antiferromagnetically coupled. The effective mass in  $\text{TiO}_2$  is much lower, especially for the electrons because of a better delocalization in the conduction band.  $\text{Fe}_2\text{TiO}_5$  has an intermediate behavior between  $\text{TiO}_2$  and  $\alpha$ - $\text{Fe}_2\text{O}_3$ .

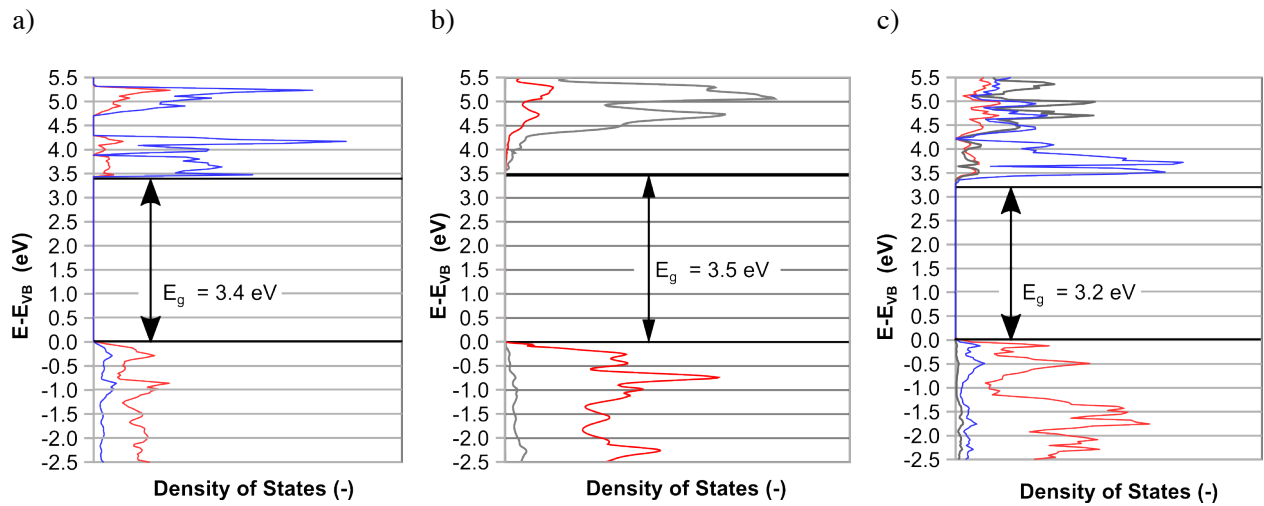


Figure 2. Computed DOS projected on the atoms of (a)  $\alpha$ - $\text{Fe}_2\text{O}_3$ , (b)  $\text{TiO}_2$ , and (c)  $\text{Fe}_2\text{TiO}_5$ . The red, grey and blue colors correspond to the projection on O, Ti and Fe atoms respectively. For magnetic compounds, only the DOS of one spin is presented since both spins are symmetric.

*Excitonic properties.* The dielectric constants are relatively high, mainly because of the vibrational contribution, stemming from the materials' ionicity. As for the effective mass, the dielectric constant of  $\text{Fe}_2\text{TiO}_5$  is intermediate between the ones of  $\alpha$ - $\text{Fe}_2\text{O}_3$  and  $\text{TiO}_2$ . Combining

the effective masses and the dielectric constants, the exciton binding energy is very different between the three materials. For  $\alpha$ -Fe<sub>2</sub>O<sub>3</sub>,  $E_b$  is larger than room thermal energy meaning that the exciton is relatively difficult to dissociate while for the two other compounds, the exciton should dissociate easily at room temperature.

	$\alpha$ -Fe <sub>2</sub> O <sub>3</sub>	TiO <sub>2</sub>	Fe <sub>2</sub> TiO <sub>5</sub>
$E_g$ (eV)	3.4	3.4	3.2
$m_{e\perp,\parallel}$ ( $m_e$ )	3.30, 3.54	0.69, 0.06	0.98, 0.96
$m_{h\perp,\parallel}$ ( $m_e$ )	1.01, 1.19	1.13, 0.15	1.36, 1.59
$\epsilon_r$ { $\epsilon_\infty$ , $\epsilon_{vib}$ }	16.5 {5.7, 10.8}	32.0 {5.8, 26.2}	21.2 {6.3, 14.8}
$E_b$ (meV)	41	3	18

Table 2: DFT computed electronic properties  $\alpha$ -Fe<sub>2</sub>O<sub>3</sub>, TiO<sub>2</sub>, and Fe<sub>2</sub>TiO<sub>5</sub>.

These calculations and the experimental data available clearly highlight their interest for this work. The strength of TiO<sub>2</sub> is in its very good electronic properties, except for the bandgap. Contrary to TiO<sub>2</sub>, hematite has a very adapted bandgap but is unadapted in terms of the other electronic properties. Finally, Fe<sub>2</sub>TiO<sub>5</sub> has intermediate properties, inheriting the well-adapted bandgap from  $\alpha$ -Fe<sub>2</sub>O<sub>3</sub> and the good electronic properties from TiO<sub>2</sub>. For these reasons, it is interesting to study experimentally the PEC properties of each material individually as well as in combination with the others.

## 3.2 Experimental Results

### 3.2.1 Nanoparticle characterizations

Aqueous solution chemistry of Ti(IV) and Fe(III) metal ions is now rather well understood when studied separately.<sup>66-73</sup> Much less is known about the ternary Ti-Fe-O diagram when

dealing with nanoparticle synthesis in water.<sup>74-76</sup> In the 2-6 pH range, both metal ions first form an amorphous or very poorly organized hydroxide precipitate. Consequently, we used a subsequent microwave assisted hydrothermal treatment to enable the oxide crystallization. pH values strongly impact the nature of the stabilized phase. Particularly, low pH yields phase mixtures containing brookite and anatase polymorphs (*cf.* Table SI-1). In the following, we focused on samples prepared at pH 6 and monitored the structural dependence on the iron content. The obtained crystallized compounds were analyzed by XRD analysis. The evolution of the XRD patterns as a function of the Fe content is shown in Figure 3.

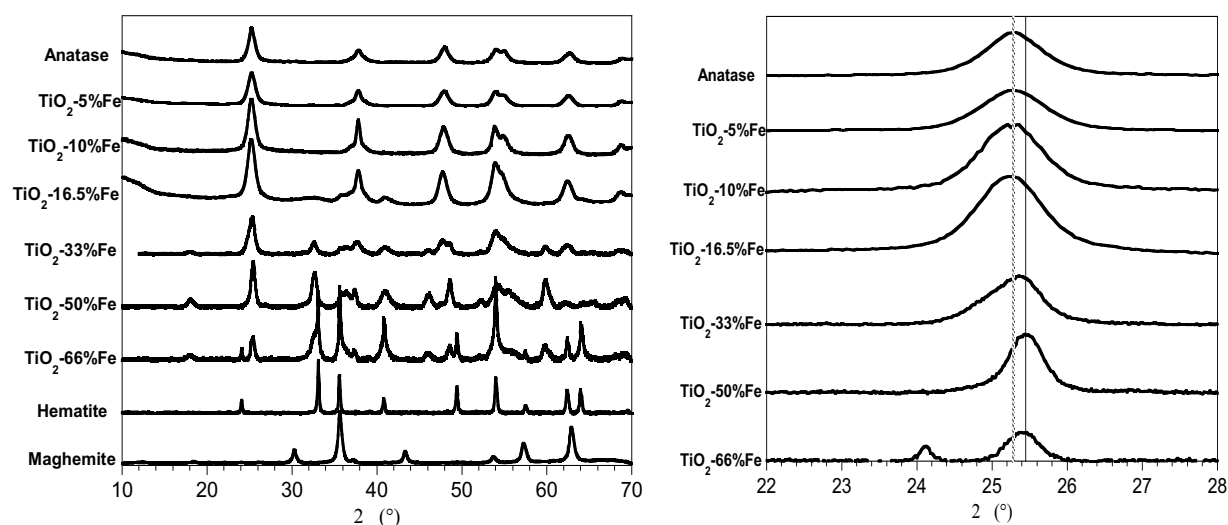


Figure 3: X-Ray diffraction patterns of pure phase  $\text{TiO}_2$  anatase  $\alpha\text{-Fe}_2\text{O}_3$  and  $\gamma\text{-Fe}_2\text{O}_3$ , and  $\text{TiO}_2$ - $x\%$ Fe composites.

X-ray diffraction analysis shows a strong structural dependence on the iron content as well as broad lines indicating the formation of nanosized particles. The  $\text{TiO}_2$  rutile structure was observed in none of the experiments, which is in good agreement with published results.<sup>77</sup> For low iron contents, i.e.  $< 10\%$ , only  $\text{TiO}_2$  anatase could be detected as crystalline phase.



Increasing the Fe ratio renders the phase identification more complex owing to numerous phases occurring in the Ti-Fe-O system. Moreover, iron doping has shown to favor the brookite  $\text{TiO}_2$  polymorph at the expense of the anatase.<sup>22, 26</sup> For %Fe higher than 10, XRD patterns strongly evolve, indicating a phase transition which becomes more obvious in  $\text{TiO}_2$ -33%Fe. A peak at around  $18^\circ$  ( $2\theta$ ) appears which can be assigned to orthorhombic  $\text{Fe}_2\text{TiO}_5$  which has a pseudo-brookite structure and eventually to a monoclinic polytype  $\text{Fe}_2\text{TiO}_5$ .<sup>78, 79</sup> Nevertheless, for the latter, the main line is absent from the XRD pattern. While increasing the Fe ratio to 50% seems to enable the preparation of a single phase of orthorhombic  $\text{Fe}_2\text{TiO}_5$ , the absence of the monoclinic variety cannot be completely ruled out. Moreover, pure  $\text{Fe}_2\text{TiO}_5$  is expected in  $\text{TiO}_2$ -66%Fe only. However, with that iron ratio, hematite is clearly detected by XRD.

Structural analyses were further conducted using synchrotron X-ray ( $\lambda = 0.2128 \text{ \AA}$ ) scattering measurements from which we obtained the pair distribution function (PDF). PDFs are indeed particularly well adapted to study nanostructured materials as they provide a histogram of all the atom-atom (pair) distances within the sample independently of its crystalline state.<sup>80</sup>

The PDF of  $\text{TiO}_2$ -50%Fe was fitted using different structural models of  $\text{Fe}_2\text{TiO}_5$  (orthorhombic pseudo-brookite with random Fe distribution in the metal sites<sup>61</sup> or ordered monoclinic structure<sup>78</sup>). The fitting using solely the pseudo-brookite type structure largely failed in reproducing the PDF data. A good fit to the PDF data was only obtained using the two polymorphs of  $\text{Fe}_2\text{TiO}_5$ . The goodness of the fit could be further increased to  $R_w = 21.6 \%$  [1-20  $\text{\AA}$ ] by the addition of a third minor phase consisting of  $\text{TiO}_2$  anatase (Figure 4). The contributions of the orthorhombic and monoclinic phases of  $\text{Fe}_2\text{TiO}_5$  to the PDF data (Figure 4) clearly indicate the co-existence of both phases.

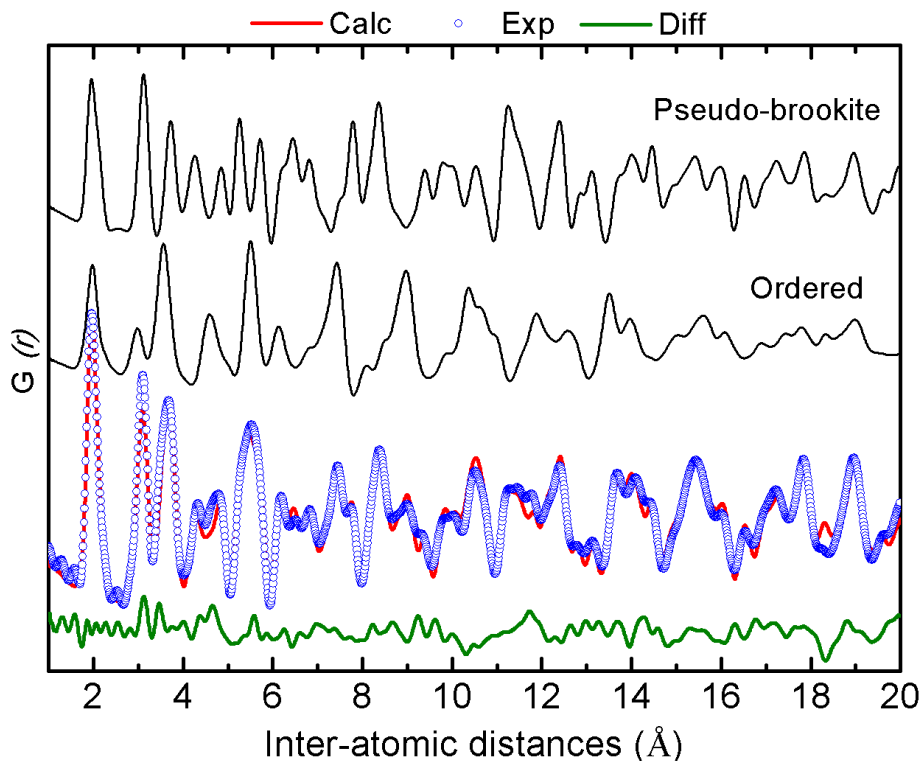


Figure 4. PDF refinement of  $\text{TiO}_2\text{-50\%Fe}$  ( $R_w = 21.6\%$ ). Individual PDF contributions of the pseudo-brookite and ordered phase of  $\text{Fe}_2\text{TiO}_5$  (black curves) extracted from the refinement.

The structural parameters of  $\text{Fe}_2\text{TiO}_5$  phases obtained by PDF refinement and their polyhedron representations are presented in Table 3 and Figure SI-2a respectively. The starting structural models of both  $\text{Fe}_2\text{TiO}_5$  polytypes were based on structures resolved by Grey and Drofenik for the orthorhombic and monoclinic phases, respectively.<sup>78, 79</sup> The atomic occupancy was fixed to initial values due to the similar X-ray scattering intensity of iron and titanium atoms. The orthorhombic structure is composed of randomly distributed  $\text{TiO}_6$  and  $\text{FeO}_6$  octahedra featuring an edge-sharing configuration. In the monoclinic phase, iron and titanium occupy the 8f and 4a Wyckoff sites, respectively, forming a network with both edge and corner-sharing octahedra. While unit cell parameters of the pseudo-brookite match those of literature data (within the

estimated standard deviation), those of the monoclinic structure significantly deviate from the reference sample (*cf.* values in italics in Table 3) obtained by the high-temperature solution method as reported by Drofenik.<sup>79</sup> The resulting changes in unit cell parameters explained the difficulty to detect this phase by conventional XRD since the most intense reflections were found to be superposed on the pseudo-brookite reflections. Moreover, the origin of the unit cell parameters variation might be a size effect and/or non-stoichiometry. Quantitative phase analysis deduced from PDF refinement indicates a total occurrence of 61-62% of Fe in contrary to the 50% used in the synthesis protocol, which indicates that (i) some titanium ions did not precipitate and that (ii) samples exhibit non-stoichiometric features.

<i>Lattice system</i>	<i>Orthorhombic</i>	<i>Monoclinic</i>
Space group	<i>C c m m</i>	<i>C 2/c</i>
Unit cell parameters (Å)	9.77(1), 9.7933 3.744(4), 3.7299 9.94(1), 9.9757	9.67(1), <i>10.1010</i> 5.02(1), <i>5.0370</i> 7.17(1), <i>7.0240</i> $\beta = 110.782^\circ$ , <i>110.9^\circ</i>
Wyckoff site, atom, atomic coordinates, occupancy	4c, Fe (0.812(1),0,0.25), 0.667 4c, Ti (0.812(1),0,0.25), 0.333 8f, Fe (0.140(1), 0, 0.0639(8)), 0.667 8f, Ti (0.140(1), 0, 0.0639(8)), 0.333 4c, O (0.248(4), 0, 0.25), 1 8f, O (0.056(3), 0, 0.887(3)), 1 8f, O (0.307(2), 0, 0.931(4)), 1	8f, Fe(0.385(2), -0.004(6), 0.267(2)), 1 4a, Ti(0,0,0), 1 8f, O(0.193(5),0.18(1), 0.160(8)), 1 8f, O(0.428(4), 0.15(1), 0.568(6)), 1 4e, O(0, 0.17(1), 0.75), 1

Table 3. Structural parameters of Fe<sub>2</sub>TiO<sub>5</sub> phases obtained by PDF analysis. Values in italics refer to reference literature data.

PDF refinements conducted on the TiO<sub>2</sub>-10-to-66%Fe series indicate that both Fe<sub>2</sub>TiO<sub>5</sub> polymorphs can be detected even at low Fe content, *i.e.* 10%, - both phases are present in almost equal proportions regardless of Fe content. Quantitative Fe content analysis (*cf.* Figure SI-2c) by

PDF refinement follows the nominal composition used during the synthesis. Slight deviations can be observed at high Fe content which, as mentioned above, can be due to non-stoichiometry. However, the chemical composition measurements determined with Inductively Coupled Plasma Mass Spectrometry (ICP-MS) and EDX on the different samples yielded values very close to the initial ratio with an error below 1 at.%. A recent study has shown that the pseudo-brookite phase may have more Ti than the exact composition  $\text{Fe}_2\text{TiO}_5$ , without significant conversion of ferric ions into ferrous ones.<sup>81</sup> Indeed, the removal of Fe(III) that lower the 2 to 1 Fe/Ti stoichiometry can be compensated by oxygen defects. Mössbauer experiments reported in Figure SI-3 confirmed that only ferric ions are present in the material. More precisely, three sites are observed upon deconvolution of the spectrum that can be attributed to the 4c and 8f sites of the orthorhombic structure<sup>26, 82</sup> and to the 8f site of the monoclinic one, in good agreement with PDF data.<sup>79</sup>

The diffractograms of phase pure  $\text{TiO}_2$  anatase,  $\alpha\text{-Fe}_2\text{O}_3$  (hematite) and  $\gamma\text{-Fe}_2\text{O}_3$  (maghemite) are also reported in Figure 3 and all diffraction peaks could be indexed according to the corresponding reference cards (JCPDS 00-021-1272, 00-033-0664 and 01-039-1346 respectively). The  $\gamma\text{-Fe}_2\text{O}_3$  maghemite diffractogram resembles that of the  $\gamma\text{-Fe}_3\text{O}_4$  magnetite. However, the brown color of the sample is in disagreement with a mixed iron oxide and all metal atoms are fully oxidized.

The presence of amorphous or very small crystalline nanoparticles was also studied through TEM. Selected micrographs corresponding to the phase pure samples and the  $\text{TiO}_2\text{-x}\%\text{Fe}$  series are reported in Figure 5. Micrographs of samples obtained at pH other than 6 are reported in Figure SI-4. The first overview of the TEM images confirms that the particle size is about 20 nm

except for hematite nanoparticle size that is closer to 100 nm. More precisely, the anatase particles with low iron content exhibit two slightly different morphologies: square bipyramids and small rods as already described in a previous article.<sup>83</sup> With increasing iron content, the TiO<sub>2</sub> small rods population becomes predominant and the rods' aspect ratio also increases. HRTEM and dark field images confirmed that there is almost no amorphous phase up to 10 at.% Fe. At 16.5 and 33 at.% Fe (figure 5d and 5e), an amorphous or poorly crystalline phase is observed around crystalline anatase nanoparticles. In those two micrographs it is difficult to distinguish pseudo-brookite nanoparticles from anatase ones. The TiO<sub>2</sub>-50%Fe sample (figure 5f) seems to present two different nanoparticles morphologies with rods and spheres. However, lattice fringes analyses on HRTEM images reported in Figure SI-5 indicate that the two observed projections may correspond to the same 3D object: a thick disk with the small dimension being parallel to the (010) plane. The mean particle thickness is 10 nm and the mean diameter ~30 nm. Another explanation for the two morphologies may be the presence of two different Fe<sub>2</sub>TiO<sub>5</sub> phases as observed in PDF analysis. No significant amorphous domains or small crystalline anatase nanoparticles could be detected on TEM micrographs. However, this does not imply that they are necessarily absent in the whole sample as they are detected in the PDF study. At even higher iron content (TiO<sub>2</sub>-66%Fe in Figure 5g) the pseudo-brookite nano-disks are thinner and larger. In addition, small quantities of large hematite rhombohedra with a length of about 300 nm can be observed (see Figure SI-6). The hematite nanoparticles synthesized as pure phase do not have that rhombohedral shape, but rather a round shape with sizes ranging from 50 to 300 nm. The maghemite nanoparticles also display a round shape without a clearly exposed family of facets and the particle size distribution is rather monodisperse at 10 nm in diameter.

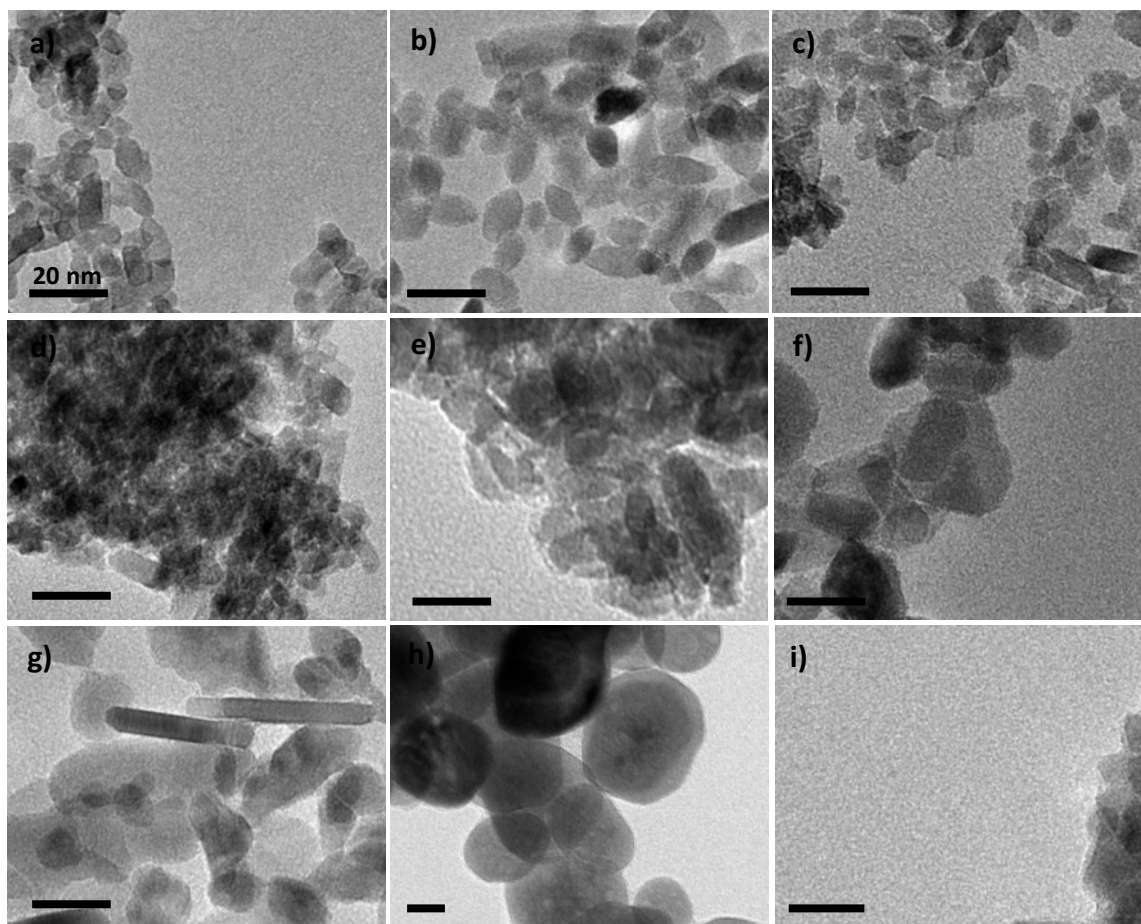


Figure 5: Transmission electron micrographs of a) pure  $\text{TiO}_2$ , b)  $\text{TiO}_2$ -5%Fe, c)  $\text{TiO}_2$ -10%Fe, d)  $\text{TiO}_2$ -16,5%Fe, e)  $\text{TiO}_2$ -33%Fe, f)  $\text{TiO}_2$ -50%Fe, g)  $\text{TiO}_2$ -66%Fe, g)  $\alpha\text{-Fe}_2\text{O}_3$  and h)  $\gamma\text{-Fe}_2\text{O}_3$ . All micrographs present the same scale bar of 20 nm.

### 3.1.2 Electrochemical characterization

Pure nanoparticles Fe-doped  $\text{TiO}_2$  anatase,  $\text{Fe}_2\text{TiO}_5$  pseudo-brookite and a mechanical mixture of  $\text{TiO}_2$ , and/or  $\text{Fe}_2\text{O}_3$  and/or  $\text{Fe}_2\text{TiO}_5$  were deposited onto FTO substrates to fabricate photoelectrodes. The synthesis procedure was described in section 2.1.3. and in Figure SI-1. An example of the microstructure created for these photoelectrodes is reported in Figure SI-1. The photoelectrodes are composed of nanoparticles delineating a mesoporous network. The thickness

determined by cross-section SEM analyses is  $\sim 30 \mu\text{m}$ . The electrochemical performances of the as-synthesized photoelectrodes of  $\text{TiO}_2$ -based nanoparticles with various iron contents are studied at  $\text{pH} = 14$  in  $1 \text{ mol}\cdot\text{L}^{-1}$  of  $\text{NaOH}$ , conditions favorable for water oxidation. First, we compare the electroactivity to water oxidation of  $\text{TiO}_2$ -based photoelectrodes ( $\text{TiO}_2$ - $x\%$ Fe with  $x = 2, 10$  and  $33$ ), as shown in Figure 6. The cyclic voltammogram shows that  $\text{TiO}_2$ -2%Fe has the lowest onset potential ( $V_{\text{on}} = \sim 0.85 \text{ V vs. RHE}$ ), while for  $\text{TiO}_2$ -33%Fe a negligible current is flowing through the cell up to an applied potential of  $1.6 \text{ V vs RHE}$ . The potential for the water oxidation reaction is at  $1.23 \text{ V}$  versus RHE, which means overpotentials of  $0.5 \text{ V}$  and  $0.7 \text{ V}$  at  $200 \mu\text{A}\cdot\text{cm}^{-2}$  for  $\text{TiO}_2$ -2%Fe and  $\text{TiO}_2$ -10%Fe respectively are required. Doping  $\text{TiO}_2$  with iron increases the photocurrent mainly at low potential, as can be seen in Figure 6. This observation is consistent with the explanation that the photocurrent is limited by trap states present at the electrode/electrolyte interface.<sup>84</sup> For unmodified  $\text{TiO}_2$ , electrons in the CB may be injected into the surface states at low potentials while they are more strongly driven away from the surface at higher applied potentials, disabling the electrons from reaching the surface states. Doping  $\text{TiO}_2$  with iron narrows the band gap, which should favor the photocurrent density (see Figure SI-7a). For 10% and more specifically 2% of Fe doping in  $\text{TiO}_2$  anatase structure it seems that additional discrete energy levels were added in the band gap. For higher concentration it is more like a combination of different contributions presenting different bandgap. All in all, the current density for  $\text{TiO}_2$ -2%Fe is  $\sim 200$  times higher than the one for  $\text{TiO}_2$ ,  $\text{TiO}_2$ -10%Fe and  $\text{TiO}_2$ -33%Fe at  $1 \text{ V vs. RHE}$ , where  $1 \text{ V}$  is close to a typical operating voltage when using this anode in conjunction with a single junction amorphous silicon solar cell. The improved  $JV$  characteristic is a sign that Fe doping  $\text{TiO}_2$  is beneficial since its presence enhances the oxidative power of the photoelectrodes.

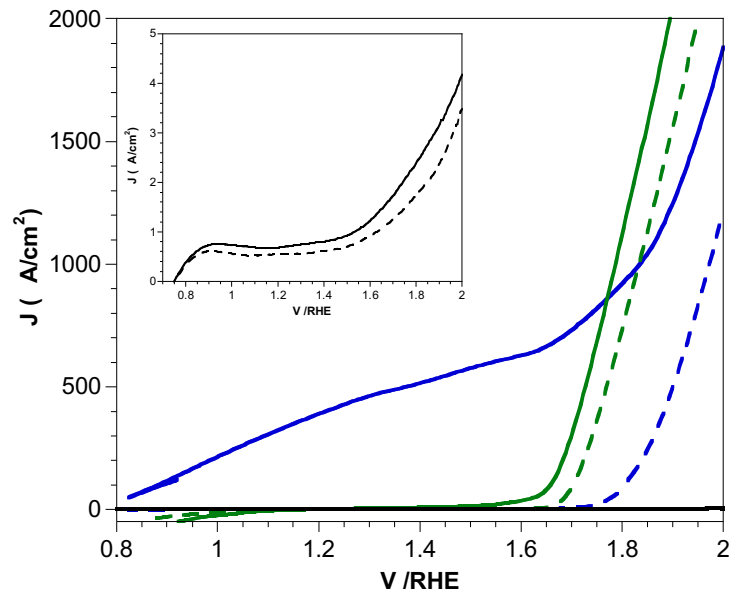


Figure 6. *JV* curve for TiO<sub>2</sub>-2%Fe (blue), TiO<sub>2</sub>-10%Fe (green) and TiO<sub>2</sub>-33%Fe (black and enlarged in the insert). Dark curves are reported and correspond to dotted lines. Measurements are performed at 20 mV·s<sup>-1</sup> and 1 M NaOH, pH = 14.

A more detailed look at the voltamogram at low potentials for TiO<sub>2</sub>-33%Fe reveals that the photocurrent increased starting at an onset potential at 0.75 V vs. RHE and that the increase of the photocurrent is more pronounced at higher potential, i.e. 1.6 V vs. RHE. This behavior can be linked to the fact that at low applied potentials (close to flat band potential), a dramatic electron/hole pair recombination is observed, *i.e.*, the photogenerated holes have trouble to reach the semiconductor/electrolyte interface. In our photoelectrodes, sources of recombination are probably the numerous grain boundaries present in the nanostructure. At more positive potentials, the electric field created favors the electron/hole pairs separation, resulting in an increase of the photocurrent.



At this point we have compared our best monophasic photoanode  $\text{TiO}_2\text{-2\%Fe}$  with its equivalent where Ti and Fe have been precipitated as oxides separately ( $\text{TiO}_2$  anatase and  $\text{Fe}_2\text{O}_3$  hematite) and combine afterwards into a nanocomposite electrode that present the same Fe:Ti atomic ratio of 2:98 (the electrode preparation is detailed in figure SI-1). The diffuse reflectance spectra of the 2% doped  $\text{TiO}_2$  and of the composite with the same metallic composition are reported in Figure SI-7b and the two JV curves are reported in Figure SI-8. The light absorption behavior of the composite significantly differs from that of doped  $\text{TiO}_2$  for it looks like the superimposition of the anatase and hematite spectra. This means that both oxides absorb light depending on their bandgap without synergetic effect in the heterostructure while Fe doping seems to improve visible light absorbance of  $\text{TiO}_2$  anatase. The JV curves are completely different too as a significant photocurrent is observed on  $\text{TiO}_2\text{-2\%Fe}$  electrode at a potential of 1 V vs. RHE while its starts to be significant only at 1.7 V vs. RHE in the 98% $\text{TiO}_2\text{-2\%}$   $\alpha\text{-Fe}_2\text{O}_3$  electrode. With higher current density slope at higher voltage the photocurrent is still lower in the composite at 1.8 V vs. RHE with 220 C vs. 840  $\mu\text{A}\cdot\text{cm}^{-2}$  in Fe doped anatase. This definitively points out that, at that Fe:Ti ratio, the doping into a well crystallized structure gives better PEC properties than heterostructured system. Oppositely, the  $\text{TiO}_2\text{-50\%Fe}$  sample is almost completely made of well crystalline  $\text{Fe}_2\text{TiO}_5$  structures and is not PEC active. Could it be possible to combine it with other oxides to recover PEC properties ?

Then, the light driven water oxidation by nanocomposite electrodes with  $\text{Fe}_2\text{TiO}_5$  and single oxide, either  $\text{TiO}_2$  or  $\text{Fe}_2\text{O}_3$ , was monitored. To do so, nanocomposite electrodes with various compositions:  $x\text{-Fe}_2\text{TiO}_5/y\text{-TiO}_2$  or  $x\text{-Fe}_2\text{TiO}_5/y\text{-Fe}_2\text{O}_3$  were fabricated; x and y represent the weight percentage (%) of  $\text{Fe}_2\text{TiO}_5$  and pure oxides, respectively. For simplicity, Figure 7 summarizes the current density (expressed in  $\mu\text{A}\cdot\text{cm}^{-2}$ ) measured at 1.8 V vs. RHE for the

nanocomposite electrodes with various compositions. We monitored the photoactivity at this potential to ensure that all the photoanodes were photo(electro)chemically active. The JV curves of pure samples are reported in Figure SI-9.

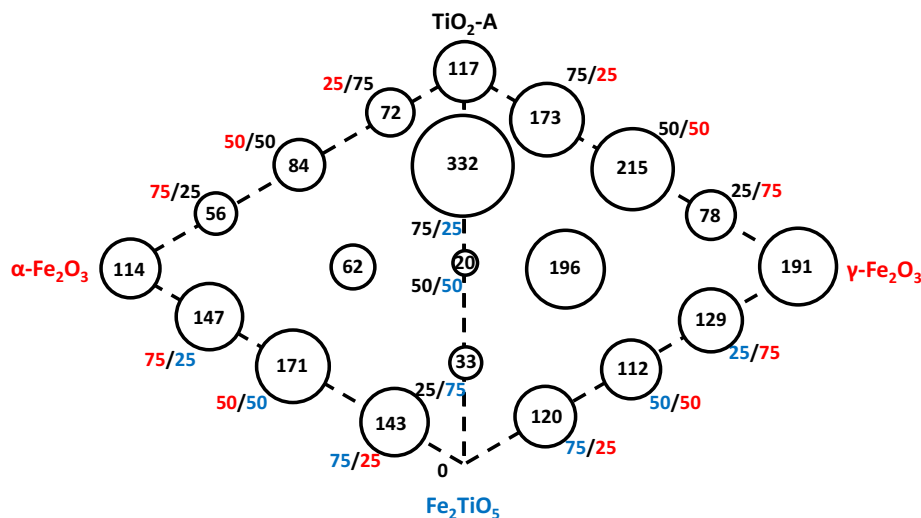


Figure 7. Photocurrents measured at 1.8 V vs. RHE and NaOH, pH = 14 for the nanocomposite photoelectrodes with various compositions. The photocurrents are given in  $\mu\text{A}\cdot\text{cm}^{-2}$  and the area of the circle is proportional to that value.

Several observations can be made: i)  $\text{Fe}_2\text{TiO}_5$  needs to be combined with either  $\text{TiO}_2$  or  $\text{Fe}_2\text{O}_3$  to achieve a high photocurrent; ii) the composite with  $\text{Fe}_2\text{TiO}_5$  and  $\text{Fe}_2\text{O}_3$  exhibits a high photocurrent for a wide range of compositions, iii) the best photocurrent for these nanocomposite electrodes is achieved for 25%  $\text{Fe}_2\text{TiO}_5$  and 75%  $\text{TiO}_2$ .

The poor electrochemical activity as well as the high onset potential (not shown here) of nanocomposite photoelectrodes with  $\text{TiO}_2$  and  $\text{Fe}_2\text{O}_3$  is consistent with findings in the literature and is due to the poor separation of holes at the semi-conductor electrolyte interface that certainly increased back electron recombination at low bias voltage.<sup>85</sup>

However, when the nanocomposite electrodes contain pseudo-brookite ( $\text{Fe}_2\text{TiO}_5/\text{Fe}_2\text{O}_3$  or  $\text{Fe}_2\text{TiO}_5/\text{TiO}_2$ ) better charge separation is achieved as photocurrents measured are higher.

For  $\text{Fe}_2\text{TiO}_5/\text{Fe}_2\text{O}_3$  nanocomposites, the heterojunction has a large effect on the charge separation process as better photocurrents are achieved for a wide range of compositions. Since both the valence and the conduction band extrema are higher in  $\text{Fe}_2\text{TiO}_5$  than in  $\text{Fe}_2\text{O}_3$  (as shown in figure 8), a straddling gap is created at the  $\text{Fe}_2\text{TiO}_5/\text{Fe}_2\text{O}_3$  n-n heterojunction. However, the photocurrent onset is still low, indicating that the amounts of long-lived surface holes are not sufficient at low bias voltage. Electron/hole recombination should then occur, probably due to the existence of numerous grain boundaries in these thick electrodes acting as sources of recombination sites. Indeed, these grain boundaries contain a large amount of defects.

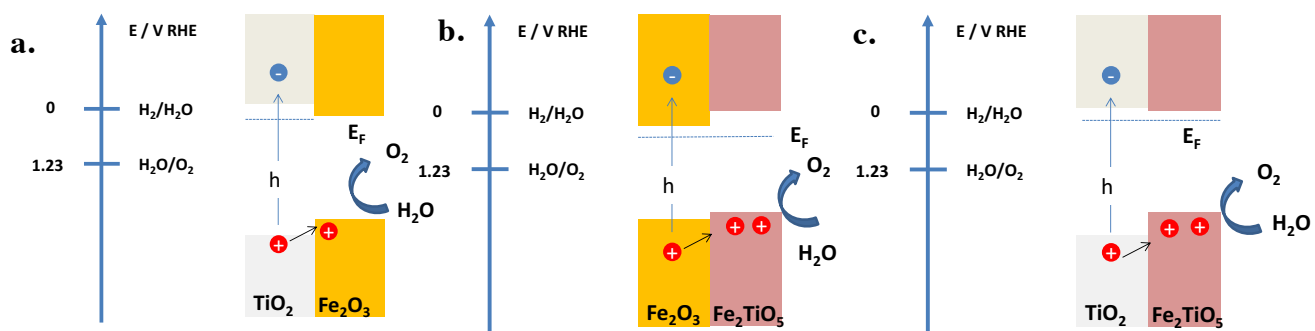


Figure 8. Charge generation, recombination, and transfer in the nanocomposite photoelectrodes studied a)  $\text{TiO}_2/\text{Fe}_2\text{O}_3$ ; b)  $\text{Fe}_2\text{O}_3/\text{Fe}_2\text{TiO}_5$  and c)  $\text{TiO}_2/\text{Fe}_2\text{TiO}_5$ . The relative VB and CB edge positions for the two oxides involved in an heterojunction is indicative of the charge separation and the place where OER may proceed. Electrons' transfer to FTO layer after charge separation is not described here.

In  $\text{TiO}_2/\text{Fe}_2\text{TiO}_5$  nanocomposites, the photocurrents depend on the composition of the electrode. Among the various nanocomposite electrodes, the one containing a high  $\text{TiO}_2$  content

(the best tested composition corresponds to 25/75  $\text{Fe}_2\text{TiO}_5/\text{TiO}_2$ ) exhibits i) the highest photocurrent and ii) the lowest onset potential (not shown here). This is an indication that the pseudo-brookite/ $\text{TiO}_2$  heterojunction has a major impact on the charge separation process. Compared to  $\text{TiO}_2/\text{Fe}_2\text{O}_3$  nanocomposite photoelectrodes,  $\text{Fe}_2\text{TiO}_5$  favors the separation of holes at the semiconductor-electrolyte interface and greatly limits the  $e^-/h^+$  recombination at low bias voltages. This is supported by recent results on hematite-titania nanocomposite photoanodes where the charge dynamics of  $\text{TiO}_2$ - $\alpha$ - $\text{Fe}_2\text{O}_3$  nanocomposite photoanodes were measured using transient absorption spectroscopy.<sup>86</sup> DFT modeling results have shown that pseudo-brookite exhibits slightly more promising electronic properties than hematite, except for hole mobility, for which reason a good catalytic efficiency is expected for  $\text{Fe}_2\text{TiO}_5$ . Consequently, the gain is rather in the efficiency of the pseudo-brookite/ $\text{TiO}_2$  heterojunction for charge separation than the electrocatalytic activity of  $\text{Fe}_2\text{TiO}_5$ . Compared to  $\text{Fe}_2\text{O}_3/\text{Fe}_2\text{TiO}_5$  nanocomposite photoelectrodes,  $\text{TiO}_2$  limits the fast charge carrier recombination due to both i) the high absorption coefficient of  $\text{TiO}_2$  compared to  $\text{Fe}_2\text{O}_3$  and ii) the higher electron mobility in  $\text{TiO}_2$  compared to  $\text{Fe}_2\text{O}_3$ .

The impact of the structure of the iron oxide on the photocurrent has been explored. We performed equivalent studies as before, but hematite was replaced by maghemite. The interest of using maghemite instead of hematite is that maghemite contains cationic vacancies that can act as sites for electron trapping, limiting electron/hole recombination. The photocurrents measured on the various photoelectrodes are summarized and reported in Figure 7. We note that nanocomposite  $\text{TiO}_2/\gamma$ - $\text{Fe}_2\text{O}_3$  photoelectrodes exhibit higher photocurrents than  $\text{TiO}_2/\alpha$ - $\text{Fe}_2\text{O}_3$ . This is probably linked to both better electron/hole separation in the photoelectrodes and holes with a longer life-time due to the presence of vacancies in  $\gamma$ - $\text{Fe}_2\text{O}_3$ . All of these facilitate the reaction with water.

In a more general comparison of the selected pure phase and the corresponding nanocomposites based on experimental and computational results, it is now possible to better explain their relative PEC activity. First pure  $\text{TiO}_2$ , that has the best photon conversion efficiency suffers from a lack of catalytically active surface sites that can exploit trapped holes before their recombination. In accontrary, pure iron oxides  $\alpha$ - and  $\gamma$ - $\text{Fe}_2\text{O}_3$  exhibit more active catalytic sites but also exhibit a lower photon conversion yield and charge mobility. The combination of  $\text{TiO}_2$  and  $\text{Fe}_2\text{O}_3$  may be beneficial in nano-heterostructures, except if the solid-solid interface favors charge recombination. Moreover, the relative amount of each phase, their structure and size should be optimized for significant PEC activity.

The ordered orthorhombic  $\text{Fe}_2\text{TiO}_5$  structure should exhibit fair PEC activity – between those of  $\text{TiO}_2$  and  $\text{Fe}_2\text{O}_3$  – according to the calculation of its electronic and structural properties. Unfortunately, our synthetic approach did not allow to produce phase pure orthorhombic  $\text{Fe}_2\text{TiO}_5$ , as a secondary monoclinic phase was detected with PDF analyses. Moreover, the iron occupancy in the pseudo-brookite structure is not fixed as proposed in the model but randomly distributed in the different metallic sites. Finally, the Fe:Ti chemical composition is slightly less than 2:1, implying oxygen defects in the structure that were not taken into account in the DFT calculations. These different points intuitively explain why the tested materials are inactive in PEC: with two phases and a random distribution of Fe atoms the  $\text{Fe}_2\text{TiO}_5$  composite is much too disordered to allow good photon conversion and charge carrier mobility. The JV curve of  $\text{Fe}_2\text{TiO}_5$  is compared in Figure SI-10 to that of a brookite sample prepared according to a procedure described in the literature.<sup>87</sup> It confirms that the brookite structure of  $\text{TiO}_2$  presents weak photocurrents ( $20 \mu\text{A}\cdot\text{cm}^{-2}$  at 1.8 V vs. RHE) and only at high bias voltage. However, it is still better that  $\text{Fe}_2\text{TiO}_5$  sample which is still inactive at such bias voltage. In accontrary, its

electrocatalytic activity may be enhanced due to the oxygen defects distorting the geometry of neighboring iron sites. Consequently the combination of small quantities of  $\text{Fe}_2\text{TiO}_5$  with a good photoharvester such as  $\text{TiO}_2$  gave the best results among heterostructured systems.

Finally, this study demonstrates that tuning the electron/hole recombination processes in the bulk electrodes, but also at the electrode/electrolyte interfaces, favors the photoactivity. This was achieved by the design of the nanocomposite photoelectrodes made of materials with different properties. However, the photocurrent achieved as well as the onset potential are lower than that those for single Fe-doped photoelectrodes (onset potential is 0.8 V vs. RHE and at 1.2 V/RHE, the photocurrent is about  $412 \mu\text{A}\cdot\text{cm}^{-2}$  and at 1.8 V/RHE is  $735 \mu\text{A}\cdot\text{cm}^{-2}$ ). This is an indication that the nanocomposite electrodes probably contain a lot of defects on the grain boundaries that act as recombination traps.

#### **4. Conclusion**

In summary, we explored the photoelectrochemical performances of different Fe-Ti oxide electrodes for water oxidation. We proposed to use *chimie douce* coupled with micro-wave stimulus to achieve pure, mono-dispersed and crystalline nanoparticles with different levels of Fe. These nanoparticles have been characterized by various techniques including X-ray diffraction, PDF analysis, HR-TEM and Mössbauer spectroscopy to monitor their structure, chemical composition and microstructure. Experimental conditions have been found and reported to achieve single phase  $\text{TiO}_2$  anatase doped with various amounts of Fe(III) up to 10 at.%, and pure  $\alpha\text{-Fe}_2\text{O}_3$  hematite or  $\gamma\text{-Fe}_2\text{O}_3$  maghemite. Most notably, two polymorphs of  $\text{Fe}_2\text{TiO}_5$  have been obtained in gentle synthesis conditions. The photoelectrochemical performances of pure Fe-doped  $\text{TiO}_2$  electrodes and nanocomposite electrodes made of  $\text{Fe}_2\text{O}_3$

or/and  $\text{Fe}_2\text{TiO}_5$  or/and  $\text{TiO}_2$  have been evaluated. We found that the electrocatalytic activity is strongly dependent on the nature of the hetero-junction and the best photocurrents are achieved for nanocomposite  $\text{Fe}_2\text{TiO}_5/\text{TiO}_2$  photoanodes with high  $\text{TiO}_2$  weight content (25/75). This increase in electrochemical performance is linked to the high absorption coefficient of  $\text{TiO}_2$  and its good electron mobility and to the higher catalytic efficiency of  $\text{Fe}_2\text{TiO}_5$  compared to  $\alpha\text{-Fe}_2\text{O}_3$ . This highlights the interest of using heterostructure to cope with poor charge carrier dynamics. However, the highest photocurrent is not achieved with heterostructured photoelectrodes but with Fe-doped  $\text{TiO}_2$  systems at a low doping content of  $\text{Fe} = 2 \text{ atom}\%$ . This demonstrates the necessity to engineer finely materials at the nanoscale to achieve both good charge carrier dynamics and high performance surface catalysis.

## ASSOCIATED CONTENT

Additional figures, including Figure SI-1: Photoanode preparation and FEG-SEM image of the cross-section of nanocomposite electrodes; Table SI-1: qualitative structure analyses of XRD patterns of Fe-Ti composites prepared at different pH; Figure SI-2: details on PDF analyses at different Fe rates and on the orthorhombic and monoclinic  $\text{Fe}_2\text{TiO}_5$  unit cell representation; Figure SI-3: Mössbauer spectrum of  $\text{TiO}_2\text{-50}\%\text{Fe}$  and its deconvolution with increasing number of  $\text{Fe}^{3+}$  sites; Figure SI-4: TEM images of selected  $\text{TiO}_2\text{-x}\%\text{Fe-pHy}$  samples; Figure SI-5: HRTEM images of  $\text{TiO}_2\text{-50}\%\text{Fe}$  sample; Figure SI-6: TEM image of  $\text{TiO}_2\text{-66}\%\text{Fe}$  sample; Figure SI-7: Diffuse reflectance spectra of different  $\text{TiO}_2\text{-x}\%\text{Fe}$  samples showing bandgap evolution as function of iron doping. Figure SI-8 to Figure SI-10 JV curves of different pure and

composite electrodes. This information is available free of charge via the Internet at <http://pubs.acs.org/>.

## AUTHOR INFORMATION

### **Corresponding Author**

Olivier Durupthy

Telephone: +33144276306, Fax: +33144271504, E-mail: [olivier.durupthy@upmc.fr](mailto:olivier.durupthy@upmc.fr)

### **Present Addresses**

†P.Sautet is now at Department of Chemical and Biomolecular engineering, University of California, Los Angeles, Los Angeles, CA 90095, United States.

### **Author Contributions**

The manuscript was written through contributions of all authors. All authors have given approval to the final version of the manuscript. ‡These authors contributed equally. (match statement to author names with a symbol)

## ACKNOWLEDGMENT

SP, CLR and OD thank MATISSE for the financial support of LD and TOTAL for the financial support of SP. STM and TLB gratefully acknowledge the computational resources



provided by *l'Institut du Développement et des Ressources en Informatique Scientifique* (IDRIS, under project x2015080609) of the *Centre Nationale de la Recherche Scientifique* (CNRS) and the Pôle Scientifique de Modélisation Numérique (PSMN) of *École Normale Supérieure de Lyon*. The work done at the Advanced Photon Source, an Office of Science User Facility operated for the U.S. Department of Energy (DOE) Office of Science by Argonne National Laboratory, was supported by the U.S. DOE under Contract No. DE-AC02-06CH11357.

## ABBREVIATIONS

AFM Anti-Ferromagnetic

CB Conduction Band

CBM Conduction Band Minimum

CNRS *Centre National de la Recherche Scientifique*

DOS Density Of States

DFT Density Functional Theory

DRS Diffuse Reflectance Spectra

EDX Energy-Dispersive X-Ray Spectroscopy

FM Ferromagnetic

NP nanoparticle

PAW Projector Augmented-Wave

PDF Pair Distribution Function

PEC Photoelectrochemical

RHE Reversible Hydrogen Electrode

TEM Transmission Electron Microscopy

TiO<sub>2</sub>-A TiO<sub>2</sub>-anatase

VB Valence Band

VBM Valence Band Maximum

XRD X-Ray Diffraction

## REFERENCES

1. Abdi, F. F.; Han, L.; Smets, A. H. M.; Zeman, M.; Dam, B.; van de Krol, R., Efficient Solar Water Splitting by Enhanced Charge Separation in a Bismuth Vanadate-Silicon Tandem Photoelectrode. *Nat. Commun.* **2013**, *4*, 2195-2195.
2. Joya, K. S.; Joya, Y. F.; Ocakoglu, K.; Van de Krol, R., Water-Splitting Catalysis and Solar Fuel Devices: Artificial Leaves on the Move. *Angew. Chemie, Int. Ed.* **2013**, *52*, 10426-10437.
3. Abdi, F. F.; Firet, N.; van de Krol, R., Efficient BiVO<sub>4</sub> Thin Film Photoanodes Modified with Cobalt Phosphate Catalyst and W-Doping. *ChemCatChem* **2013**, *5*, 490-496.
4. Gratzel, M., Photoelectrochemical Cells. *Nature* **2001**, *414*, 338-344.
5. McEvoy, J. P.; Brudvig, G. W., Water-Splitting Chemistry of Photosystem II. *Chem. Rev.* **2006**, *106*, 4455-4483.
6. Nocera, D. G., Personalized Energy: The Home as a Solar Power Station and Solar Gas Station. *ChemSuschem* **2009**, *2*, 387-390.
7. Sivula, K., Metal Oxide Photoelectrodes for Solar Fuel Production, Surface Traps, and Catalysis. *J. Phys. Chem. Lett.*, *4*, 1624-1633.
8. Hamann, T. W., Splitting Water with Rust: Hematite Photoelectrochemistry. *Dalton Trans.* **2012**, *41*, 7830-7834.
9. Gan, J.; Lu, X.; Tong, Y., Towards Highly Efficient Photoanodes: Boosting Sunlight-Driven Semiconductor Nanomaterials for Water Oxidation. *Nanoscale* **2014**, *6*, 7142-7164.

10. Sivula, K.; Le Formal, F.; Graetzel, M., Solar Water Splitting: Progress Using Hematite ( $\alpha$ -Fe<sub>2</sub>O<sub>3</sub>) Photoelectrodes. *ChemSuschem* **2011**, *4*, 432-449.
11. Barroso, M.; Pendlebury, S. R.; Cowan, A. J.; Durrant, J. R., Charge Carrier Trapping, Recombination and Transfer in Hematite Water Splitting Photoanodes. *Chem. Sci.* **2013**, *4*, 2724-2734.
12. Ginley, D. S.; Butler, M. A., Photoelectrolysis of Water Using Iron Titanate Anodes. *J. Appl. Phys.* **1977**, *48*, 2019-2021.
13. Fujishima, A.; Honda, K., Electrochemical Photolysis of Water at a Semiconductor Electrode. *Nature* **1972**, *238*, 37-38.
14. Cowan, A. J.; Tang, J.; Leng, W.; Durrant, J. R.; Klug, D. R., Water Splitting by Nanocrystalline TiO<sub>2</sub> in a Complete Photoelectrochemical Cell Exhibits Efficiencies Limited by Charge Recombination. *J. Phys. Chem. C* **2010**, *114*, 4208-4214.
15. Dholam, R.; Patel, N.; Adami, M.; Miotello, A., Hydrogen Production by Photocatalytic Water-Splitting Using Cr- or Fe-Doped TiO<sub>2</sub> Composite Thin Films Photocatalyst. *Int. J. Hydrogen Energy* **2009**, *34*, 5337-5346.
16. Tang, J.; Durrant, J. R.; Klug, D. R., Mechanism of Photocatalytic Water Splitting in TiO<sub>2</sub>. Reaction of Water with Photoholes, Importance of Charge Carrier Dynamics, and Evidence for Four-Hole Chemistry. *J. Am. Chem. Soc.* **2008**, *130*, 13885-13891.
17. Stamate, M. D., Dielectric Properties of TiO<sub>2</sub> Thin Films Deposited by a Dc Magnetron Sputtering System. *Thin Solid Films* **2000**, *372*, 246-249.
18. Le Formal, F.; Pendlebury, S. R.; Cornuz, M.; Tilley, S. D.; Grätzel, M.; Durrant, J. R., Back Electron-Hole Recombination in Hematite Photoanodes for Water Splitting. *J. Am. Chem. Soc.* **2014**, *136*, 2564-2574.
19. Yu, J. G.; Yu, H. G.; Ao, C. H.; Lee, S. C.; Yu, J. C.; Ho, W. K., Preparation, Characterization and Photocatalytic Activity of in Situ Fe-Doped TiO<sub>2</sub> Thin Films. *Thin Solid Films* **2006**, *496*, 273-280.
20. Yu, J. C.; Wang, X. C.; Fu, X. Z., Pore-Wall Chemistry and Photocatalytic Activity of Mesoporous Titania Molecular Sieve Films. *Chem. Mater.* **2004**, *16*, 1523-1530.
21. Saremi-Yarahmadi, S.; Wijayantha, K. G. U.; Tahir, A. A.; Vaidhyanathan, B., Nanostructured Ahem Electrodes for Solar Driven Water Splitting: Effect of Doping Agents on Preparation and Performance. *J. Phys. Chem. C* **2009**, *113*, 4768-4778.
22. Santos, R. d. S.; Faria, G. A.; Giles, C.; Leite, C. A. P.; Barbosa, H. d. S.; Arruda, M. A. Z.; Longo, C., Iron Insertion and Hematite Segregation on Fe-Doped TiO<sub>2</sub> Nanoparticles Obtained from Sol-Gel and Hydrothermal Methods. *ACS Appl. Mater. Interfaces* **2012**, *4*, 5555-5561.
23. Zhao, W.; Li, Y.; Zhang, M.; Chen, J.; Xie, L.; Shi, Q.; Zhu, X., Direct Microwave Hydrothermal Synthesis of Fe-Doped Titania with Extended Visible-Light Response and Enhanced H<sub>2</sub>-Production Performance. *Chem. Eng. J.* **2016**, *283*, 105-113.
24. Zhang, X.; Lei, L., Preparation of Photocatalytic Fe<sub>2</sub>O<sub>3</sub>-TiO<sub>2</sub> Coatings in One Step by Metal Organic Chemical Vapor Deposition. *Appl. Surf. Sci.* **2008**, *254*, 2406-2412.
25. Peng, L.; Xie, T.; Lu, Y.; Fan, H.; Wang, D., Synthesis, Photoelectric Properties and Photocatalytic Activity of the Fe<sub>2</sub>O<sub>3</sub>/TiO<sub>2</sub> Heterogeneous Photocatalysts. *Phys. Chem. Chem. Phys.* **2010**, *12*, 8033-8041.
26. Courtin, E.; Baldinozzi, G.; Sougrati, M. T.; Stievano, L.; Sanchez, C.; Laberty-Robert, C., New Fe<sub>2</sub>tio<sub>5</sub>-Based Nanoheterostructured Mesoporous Photoanodes with Improved Visible Light Photoresponses. *J. Mater. Chem. A* **2014**, *2*, 6567-6577.

27. Moniz, S. J. A.; Shevlin, S. A.; An, X.; Guo, Z.-X.; Tang, J., Fe<sub>2</sub>O<sub>3</sub>-TiO<sub>2</sub> Nanocomposites for Enhanced Charge Separation and Photocatalytic Activity. *Chem. Eur. J.* **2014**, *20*, 15571-15579.
28. Ahmed, M. G.; Kretschmer, I. E.; Kandiel, T. A.; Ahmed, A. Y.; Rashwan, F. A.; Bahnemann, D. W., A Facile Surface Passivation of Hematite Photoanodes with TiO<sub>2</sub> Overlayers for Efficient Solar Water Splitting. *ACS Appl. Mater. Interfaces* **2015**, *7*, 24053-24062.
29. Melissen, S.; Labat, F.; Sautet, P.; Le Bahers, T., Electronic Properties of Pb<sub>x</sub>3ch<sub>3</sub>nh<sub>3</sub> (X = Cl, Br, I) Compounds for Photovoltaic and Photocatalytic Applications. *Phys. Chem. Chem. Phys.* **2015**, *17*, 2199-2209.
30. Melissen, S.; Bahers, T. L.; Steinmann, S. N.; Sautet, P., The Relationship between Carbon Nitride Structure and Exciton Binding Energies: A Dft Perspective. *J. Phys. Chem. C.* **2015**.
31. Bhunia, M. K.; Melissen, S.; Parida, M. R.; Sarawade, P.; Basset, J.-M.; Anjum, D. H.; Mohammed, O. F.; Sautet, P.; Le Bahers, T.; Takanabe, K., Dendritic Tip-on Polytriazine-Based Carbon Nitride Photocatalyst with High Hydrogen Evolution Activity. *Chem. Mater.* **2015**, *27*, 8237-8247.
32. Le Bahers, T.; Haller, S.; Le Mercier, T.; Barboux, P., Assessing the Use of Bicus for Photovoltaic Application: From Dft to Macroscopic Simulation. *J. Phys. Chem. C* **2015**, *119*, 17585-17595.
33. Kandiel, T. A.; Anjum, D. H.; Sautet, P.; Le Bahers, T.; Takanabe, K., Electronic Structure and Photocatalytic Activity of Wurtzite Cugaas Nanocrystals and Their Zn Substitution. *J. Mater. Chem. A* **2015**, *3*, 8896-8904.
34. Pottier, A.; Cassaignon, S.; Chanéac, C.; Villain, F.; Tronc, E.; Jolivet, J.-P., Size Tailoring of TiO<sub>2</sub> Anatase Nanoparticles in Aqueous Medium and Synthesis of Nanocomposites. Characterization by Raman Spectroscopy. *J. Mater. Chem.* **2003**, *13*, 877-882.
35. Sreeja, V.; Joy, P. A., Microwave-Hydrothermal Synthesis of  $\Gamma$ -Fe<sub>2</sub>O<sub>3</sub> Nanoparticles and Their Magnetic Properties. *Mater. Res. Bull.* **2007**, *42*, 1570-1576.
36. Chupas, P. J.; Chapman, K. W.; Lee, P. L., Applications of an Amorphous Silicon-Based Area Detector for High-Resolution, High-Sensitivity and Fast Time-Resolved Pair Distribution Function Measurements. *J. Appl. Crystallogr.* **2007**, *40*, 463-470.
37. Chupas, P. J.; Qiu, X. Y.; Hanson, J. C.; Lee, P. L.; Grey, C. P.; Billinge, S. J. L., Rapid-Acquisition Pair Distribution Function (Ra-Pdf) Analysis. *J. Appl. Crystallogr.* **2003**, *36*, 1342-1347.
38. Hammersley, A. P.; Svensson, S. O.; Hanfland, M.; Fitch, A. N.; Hausermann, D., Two-Dimensional Detector Software: From Real Detector to Idealised Image or Two-Theta Scan. *High Pressure Res.* **1996**, *14*, 235-248.
39. Qiu, X.; Thompson, J. W.; Billinge, S. J. L., Pdfgetx2: A Gui-Driven Program to Obtain the Pair Distribution Function from X-Ray Powder Diffraction Data. *J. Appl. Crystallogr.* **2004**, *37*, 678.
40. Farrow, C. L.; Juhas, P.; Liu, J. W.; Bryndin, D.; Bozin, E. S.; Bloch, J.; Proffen, T.; Billinge, S. J. L., Pdfit2 and Pdfgui: Computer Programs for Studying Nanostructure in Crystals. *J. Phys.: Condens. Matter* **2007**, *19*.
41. Dovesi, R., et al., Crystal14: A Program for the Ab Initio Investigation of Crystalline Solids. *Int. J. Quant. Chem.* **2014**, *114*, 1287-1317.
42. Dovesi, R., et al., *Crystal14 User's Manual (University of Torino)*, 2014.

43. Catti, M.; Valerio, G.; Dovesi, R., Theoretical Study of Electronic, Magnetic, and Structural Properties of Alpha -Fe<sub>2</sub>O<sub>3</sub> (Hematite). *Phys. Rev. B* **1995**, *51*, 7441-7450.
44. Sophia, G.; Baranek, P.; Sarrazin, C.; Rérat, M.; Dovesi, R., First-Principles Study of the Mechanisms of the Pressure-Induced Dielectric Anomalies in Ferroelectric Perovskites. *Phase Trans.* **2013**, *86*, 1069-1084.
45. Adamo, C.; Barone, V., Toward Reliable Density Functional Methods without Adjustable Parameters: The Pbe0 Model. *J. Chem. Phys.* **1999**, *110*, 6158-6170.
46. Monkhorst, H. J.; Pack, J. D., Special Points for Brillouin-Zone Integrations. *Phys. Rev. B* **1976**, *13*, 5188-5192.
47. Heyd, J.; Scuseria, G. E.; Ernzerhof, M., Hybrid Functionals Based on a Screened Coulomb Potential. *J. Chem. Phys.* **2003**, *118*, 8207-8215.
48. Heyd, J.; Scuseria, G. E.; Ernzerhof, M., Erratum: Hybrid Functionals Based on a Screened Coulomb Potential *J. Chem. Phys.* **118**, 8207 (2003)*J. Chem. Phys.* **2006**, *124*, 219906-219906.
49. Krukau, A. V.; Vydrov, O. A.; Izmaylov, A. F.; Scuseria, G. E., Influence of the Exchange Screening Parameter on the Performance of Screened Hybrid Functionals. *J. Chem. Phys.* **2006**, *125*, 224106-224106.
50. Barone, V.; Hod, O.; Peralta, J. E.; Scuseria, G. E., Accurate Prediction of the Electronic Properties of Low-Dimensional Graphene Derivatives Using a Screened Hybrid Density Functional. *Acc. Chem. Res.* **2011**, *44*, 269-279.
51. Henderson, T. M.; Paier, J.; Scuseria, G. E., Accurate Treatment of Solids with the Hse Screened Hybrid. *Phys. Status Solidi (B)* **2011**, *248*, 767-774.
52. Le Bahers, T.; Rérat, M.; Sautet, P., Semiconductors Used in Photovoltaic and Photocatalytic Devices: Assessing Fundamental Properties from Dft. *J. Phys. Chem. C* **2014**, *118*, 5997-6008.
53. Noel, Y.; Zicovich-Wilson, C. M.; Civalleri, B.; D'Arco, P.; Dovesi, R., Polarization Properties of Zno and Beo: An Ab Initio Study through the Berry Phase and Wannier Functions Approaches. *Phys. Rev. B* **2001**, *65*, 14111-14111.
54. Ferrero, M.; Rerat, M.; Orlando, R.; Dovesi, R., Coupled Perturbed Hartree-Fock for Periodic Systems: The Role of Symmetry and Related Computational Aspects. *J. Chem. Phys.* **2008**, *128*, 014110-014110
55. Ferrero, M.; Rerat, M.; Orlando, R.; Dovesi, R., The Calculation of Static Polarizabilities of 1-3d Periodic Compounds. The Implementation in the Crystal Code. *J. Comput. Chem.* **2007**, *29*, 1450-1459.
56. Ferrero, M.; Rerat, M.; Kirtman, B.; Dovesi, R., The Calculation of Static Polarizabilities of 1-3d Periodic Compounds. The Implementation in the Crystal Code. *J. Chem. Phys.* **2008**, *129*, 244110-244110.
57. Mele, E. J., Screening of a Point Charge by an Anisotropic Medium: Anamorphoses in the Method of Images. *Am. J. Phys.* **2001**, *69*, 557-562.
58. Adelstein, N.; Neaton, J. B.; Asta, M.; De Jonghe, L. C., Density Functional Theory Based Calculation of Small-Polaron Mobility in Hematite. *Phys. Rev. B* **2014**, *89*, 245115-245115.
59. Yang, H.; Mi, W.; Bai, H.; Cheng, Y., Electronic and Optical Properties of New Multifunctional Materials Via Half-Substituted Hematite: First Principles Calculations. *RSC Adv.* **2012**, *2*, 10708-10716.

60. Howard, C. J.; Sabine, T. M.; Dickson, F., Structural and Thermal Parameters for Rutile and Anatase. *Acta Crystallogr. Sect. B* **1991**, *47*, 462-468.
61. Guo, W. Q.; Malus, S.; Ryan, D. H.; Altounian, Z., Crystal Structure and Cation Distributions in the  $\text{FeTi}_2\text{O}_5\text{-Fe}_2\text{TiO}_5$  Solid Solution Series. *J. Phys.: Condens. Matter* **1999**, *11*, 6337-6346.
62. Pozun, Z. D.; Henkelman, G., Hybrid Density Functional Theory Band Structure Engineering in Hematite. *J. Chem. Phys.* **2011**, *134*, 224706-224706.
63. Dudarev, S. L.; Botton, G. A.; Savrasov, S. Y.; Humphreys, C. J.; Sutton, A. P., Electron-Energy-Loss Spectra and the Structural Stability of Nickel Oxide: An Lsda+U Study. *Phys. Rev. B* **1998**, *57*, 1505-1509.
64. Huda, M. N.; Walsh, A.; Yan, Y.; Wei, S.-H.; Al-Jassim, M. M., Electronic, Structural, and Magnetic Effects of 3d Transition Metals in Hematite. *J. Appl. Phys.* **2010**, *107*, 123712-123712.
65. Tang, H.; Yin, W.-J.; Matin, M. A.; Wang, H.; Deutsch, T.; Al-Jassim, M. M.; Turner, J. A.; Yan, Y., Titanium and Magnesium Co-Alloyed Hematite Thin Films for Photoelectrochemical Water Splitting. *J. Appl. Phys.* **2012**, *111*, 073502-073502.
66. Cassaignon, S.; Koelsch, M.; Jolivet, J.-P., Selective Synthesis of Brookite, Anatase and Rutile Nanoparticles: Thermolysis of  $\text{TiCl}_4$  in Aqueous Nitric Acid. *J. Mater. Sci.* **2007**, *42*, 6689-6695.
67. Cassaignon, S.; Koelsch, M.; Jolivet, J.-P., From  $\text{TiCl}_3$  to  $\text{TiO}_2$  Nanoparticles (Anatase, Brookite and Rutile): Thermohydrolysis and Oxidation in Aqueous Medium. *J. Phys. Chem. Solids* **2007**, *68*, 695-700.
68. Pottier, A. S.; Cassaignon, S.; Chaneac, C.; Villain, F.; Tronc, E.; Jolivet, J. P., Size Tailoring of  $\text{TiO}_2$  Anatase Nanoparticles in Aqueous Medium and Synthesis of Nanocomposites. Characterization by Raman Spectroscopy. *J. Mater. Chem.* **2003**, *13*, 877-882.
69. Jolivet, J. P.; Chaneac, C.; Tronc, E., Iron Oxide Chemistry. From Molecular Clusters to Extended Solid Networks. *Chem. Commun.* **2004**, 481-487.
70. Pottier, A.; Chaneac, C.; Tronc, E.; Mazerolles, L.; Jolivet, J. P., Synthesis of Brookite  $\text{TiO}_2$  Nanoparticles by Thermolysis of  $\text{TiCl}_4$  in Strongly Acidic Aqueous Media. *J. Mater. Chem.* **2001**, *11*, 1116-1121.
71. Vayssieres, L.; Chaneac, C.; Tronc, E.; Jolivet, J. P., Size Tailoring of Magnetite Particles Formed by Aqueous Precipitation: An Example of Thermodynamic Stability of Nanometric Oxide Particles. *J. Colloid Interf. Sci.* **1998**, *205*, 205-212.
72. Jolivet, J.-P.; Tronc, E.; Chaneac, C., Iron Oxides: From Molecular Clusters to Solid. A Nice Example of Chemical Versatility. *C.R. Geosci.* **2006**, *338*, 488-497.
73. Li, L.; Fan, M. H.; Brown, R. C.; Van Leeuwen, J. H.; Wang, J. J.; Wang, W. H.; Song, Y. H.; Zhang, P. Y., Synthesis, Properties, and Environmental Applications of Nanoscale Iron-Based Materials: A Review. *Crit. Rev. Env. Sci. Technol.* **2006**, *36*, 405-431.
74. Adan, C.; Bahamonde, A.; Fernandez-Garcia, M.; Martinez-Arias, A., Structure and Activity of Nanosized Iron-Doped Anatase  $\text{TiO}_2$  Catalysts for Phenol Photocatalytic Degradation. *Appl. Catal., B* **2007**, *72*, 11-17.
75. Ambrus, Z.; Balazs, N.; Alapi, T.; Wittmann, G.; Sipos, P.; Dombi, A.; Mogyorosi, K., Synthesis, Structure and Photocatalytic Properties of Fe(III)-Doped  $\text{TiO}_2$  Prepared from  $\text{TiCl}_3$ . *Appl. Catal., B* **2008**, *81*, 27-37.
76. Khaleel, A., Sol-Gel Synthesis, Characterization, and Catalytic Activity of Fe(II) Titanates. *Colloids Surf., A* **2009**, *346*, 130-137.

77. Dufour, F.; Cassaignon, S.; Durupthy, O.; Colbeau-Justin, C.; Chanéac, C., Do Tio<sub>2</sub> Nanoparticles Really Taste Better When Cooked in a Microwave Oven? *Eur. J. Inorg. Chem.* **2012**, 2707-2715.
78. Grey, I. E.; Li, C.; Ness, T., Nonstoichiometric Li-Pseudobrookite(Ss) in the Li<sub>2</sub>o-Fe<sub>2</sub>o<sub>3</sub>-Tio<sub>2</sub> System. *J. Solid State Chem.* **1998**, *141*, 221-228.
79. Drofenik, M.; Golic, L.; Hanzel, D.; Krasevec, V.; Prodan, A.; Bakker, M.; Kolar, D., A New Monoclinic Phase in the Fe<sub>2</sub>o<sub>3</sub>-Tio<sub>2</sub> System .1. Structure Determination and Mossbauer-Spectroscopy. *J. Solid State Chem.* **1981**, *40*, 47-51.
80. Billinge, S. J. L.; Kanatzidis, M. G., Beyond Crystallography: The Study of Disorder, Nanocrystallinity and Crystallographically Challenged Materials with Pair Distribution Functions. *Chem. Commun.* **2004**, 749-760.
81. Seitz, G.; Penin, N.; Decoux, L. a.; Wattiaux, A.; Duttine, M.; Gaudon, M., Near the Ferric Pseudobrookite Composition (Fe<sub>2</sub>tio<sub>5</sub>). *Inorg. Chem.* **2016**, *55*, 2499-2507.
82. Hirano, M.; Joji, T.; Inagaki, M., Direct Formation of Iron(Iii)-Doped Titanium Oxide (Anatase) by Thermal Hydrolysis and Its Structural Property. *J. Am. Ceram. Soc.* **2004**, *87*, 35-41.
83. Dufour, F.; Pigeot-Remy, S.; Durupthy, O.; Cassaignon, S.; Ruaux, V.; Torelli, S.; Mariey, L.; Maugé, F.; Chanéac, C., Morphological Control of Tio<sub>2</sub> Anatase Nanoparticles: What Is the Good Surface Property to Obtain Efficient Photocatalysts? *Appl. Catal., B* **2015**, *174-175*, 350-360.
84. Le Formal, F.; Sivula, K.; Graetzel, M., The Transient Photocurrent and Photovoltage Behavior of a Hematite Photoanode under Working Conditions and the Influence of Surface Treatments. *J. Phys. Chem. C* **2012**, *116*, 26707-26720.
85. Kuang, S.; Yang, L.; Luo, S.; Cai, Q., Fabrication, Characterization and Photoelectrochemical Properties of Fe<sub>2</sub>o<sub>3</sub> Modified Tio<sub>2</sub> Nanotube Arrays. *Appl. Surf. Sci.* **2009**, *255*, 7385-7388.
86. Cowan, A. J.; Barnett, C. J.; Pendlebury, S. R.; Barroso, M.; Sivula, K.; Graetzel, M.; Durrant, J. R.; Klug, D. R., Activation Energies for the Rate-Limiting Step in Water Photooxidation by Nanostructured  $\alpha$ -Fe<sub>2</sub>o<sub>3</sub> and Tio<sub>2</sub>. *J. Am. Chem. Soc.* **2011**, *133*, 10134-10140.
87. Magne, C.; Dufour, F.; Labat, F.; Lancel, G.; Durupthy, O.; Cassaignon, S.; Pauporté, T., Effects of Tio<sub>2</sub> Nanoparticle Polymorphism on Dye-Sensitized Solar Cell Photovoltaic Properties. *J. Photochem. Photobiol., A* **2012**, *232*, 22-31.

Insert Table of Contents Graphic and Synopsis Here

